Journal of Physics D:
Applied Physics

PAPER • **OPEN ACCESS**

Influence of an ultrathin Mn ‘spy layer’ on the static and dynamic magnetic coupling within FePt/NiFe bilayers

To cite this article: David G Newman *et al* 2025 *J. Phys. D: Appl. Phys.* **58** 045002

OPEN ACCESS
IOP Publishing
Journal of Physics D: Applied Physics
J. Phys. D: Appl. Phys. **58** (2025) 045002 (11pp)
https://doi.org/10.1088/1361-6463/ad89d0

Influence of an ultrathin Mn 'spy layer' on the static and dynamic magnetic coupling within FePt/NiFe bilayers

David G Newman[1], Andreas Frisk[2], David M Burn[2], Barat Achinuq[3], Emily Heppell[2,3,4], Graham J Bowden[5], Maciej Dąbrowski[1], Gerrit van der Laan[2], Thorsten Hesjedal[2,3] and Robert J Hicken[1,*]

[1] Department of Physics and Astronomy, University of Exeter, Stocker Road, Exeter, Devon EX4 4QL, United Kingdom
[2] Diamond Light Source, Harwell Science and Innovation Campus, Fermi Ave, Didcot OX11 0DE, United Kingdom
[3] Department of Physics, University of Oxford, Parks Road, Oxford OX1 3PU, United Kingdom
[4] ISIS Neutron and Muon Source, Rutherford Appleton Laboratory, Harwell Science and Innovation Campus, Didcot OX11 0QX, United Kingdom
[5] School of Physics and Astronomy, University of Southampton, Southampton SO17 1BJ, United Kingdom

E-mail: R.J.Hicken@exeter.ac.uk

Received 22 January 2024, revised 2 October 2024
Accepted for publication 22 October 2024
Published 11 November 2024

Abstract

We explore whether insertion of an ultrathin Mn 'spy layer' within a magnetic hard/soft bilayer can enable depth-sensitive element-specific measurements of the static and dynamic magnetization, while avoiding significant disruption of the original magnetic state. MgO(110)/FePt(100 Å)/NiFe(200 Å)/Mn(t_{Mn} Å)/NiFe(200 Å) samples with Mn thicknesses of $t_{Mn} = 0$, 5, and 10 Å were fabricated by magnetron sputtering and studied by element-selective x-ray magnetic circular dichroism (XMCD), vector network analyzer ferromagnetic resonance (VNA-FMR), and x-ray detected ferromagnetic resonance (XFMR). For $t_{Mn} = 5$ Å, the magnetic reversal properties remain broadly similar to $t_{Mn} = 0$ Å. For $t_{Mn} = 10$ Å, the two NiFe layers decouple with XMCD hysteresis loops at the Mn edge showing two switching events that suggest the presence of two distinct Mn-containing regions. While the Mn moments within each region have ferromagnetic order, their relative alignment is antiparallel at high field. Analysis of the magnetic data and additional scanning transmission electron microscopy measurements point to the presence of a Mn layer at the lower NiFe/Mn interface, and the formation of a NiFeMn alloy at the upper Mn/NiFe interface. The Mn moments of the former region lie antiparallel to those of the underlying NiFe layer. The VNA-FMR data suggests that for $t_{Mn} = 5$ and 10 Å, the interfacial exchange coupling at the FePt/NiFe is suppressed and the in-plane

* Author to whom any correspondence should be addressed.

uniaxial magnetic anisotropy of the NiFe is increased, perhaps due to migration of Mn towards the buried interface. The above findings show that Mn is a problematic magnetic spy, and that a Mn thickness of less than 5 Å would be required.

Supplementary material for this article is available online

Keywords: magnetism, exchange spring, ferromagnetic resonance

1. Introduction

Magnetic hard/soft bilayers have attracted great interest due to the twisted magnetization states that they exhibit [1]. So-called exchange spring (ES) behaviour is obtained when a magnetic field is applied parallel to the easy axis of the hard layer and swept from negative saturation towards positive field values, so that the magnetization at the unpinned interface of the soft layer switches at the so-called bending field [2], while the magnetization at the interface with the hard layer remains pinned. The magnetization direction twists through the thickness of the soft layer, forming an ES. As the field is further increased to a value between the bending field and the switching field of the hard layer, the ES becomes more tightly wound. It has been demonstrated that microwave excitation [3] can reduce the switching field of the hard layer via injection of spin waves from the soft layer [4, 5], making such bilayers promising candidates for use in next generation magnetic data storage technologies, e.g. in microwave assisted magnetic recording (MAMR) devices. However, it should also be noted that the classic ES-state, described above, is not the only twisted magnetization state available to the system. A twisted state can also be set up by applying the magnetic field, again in-plane, but this time orthogonal to the easy axis of the hard layer.

For the practical exploitation of hard/soft bilayers and multilayers, it is crucial to characterize their magnetic state. Element-specific x-ray magnetic circular dichroism (XMCD) and x-ray detected ferromagnetic resonance (XFMR) are powerful methods for investigating such systems [6], however, they are only able to access the average magnetization within a particular layer and generally do not provide any depth-sensitivity. On the other hand, reflectometry ferromagnetic resonance (RFMR) can provide access to the depth-dependent variation of magnetization through a layer stack [7], but it requires a highly specialized diffraction setup. Here, the possibility of achieving depth-sensitivity in element-specific measurements of twisted magnetization states through the insertion of an ultrathin 'spy layer' is explored. An ideal spy layer will align with the magnetization of the surrounding soft layer without significantly affecting either its orientation or its dynamical response.

Due to its large atomic moment and sensitivity to the ordering of neighboring magnetic moments [8], Mn was selected as the magnetic spy layer. Further advantages are that Mn exhibits a variety of different structural phases [9] and different interfacial exchange couplings [10], which can potentially minimize detrimental effects on the host layer magnetization. In the present work, the effect of ultrathin Mn spy layers of different thickness on a FePt/NiFe bilayer has been studied.

2. Experimental details

A series of samples with the nominal structure MgO(110) substrate/FePt $L1_0$ (100 Å)/NiFe (200 Å)/Mn (t_{Mn})/NiFe (200 Å), where $t_{Mn} = 0$, 5, and 10 Å, were fabricated in a home-built magnetron sputtering system [11] with the NiFe and Mn layers grown at 200°C and the FePt grown via co-deposition of Fe and Pt at 650°C [12]. Two reference samples were also grown, the first with a thick 100 Å Mn spy layer, and the second with $t_{Mn} = 10$ Å and the FePt replaced with a 50 Å-thick Pt layer. Magnetic alloys in the $L1_0$ phase have been shown to possess large magnetocrystalline anisotropies [13], which makes them ideal candidates for the hard layer in a hard/soft bilayer system, and the FePt/NiFe structure has previously been shown to exhibit an ES state [14]. The FePt $L1_0$ layer was grown on MgO(110) so as to favor the growth of FePt(110) grains with the *c*-axis parallel to the in-plane MgO[001] direction [15]. This leads to a strong effective in-plane uniaxial anisotropy, necessary for forming a twisted magnetization state, with the magnetization pinned along the [001] direction at the FePt/NiFe interface. In the following, all crystallographic directions given are with respect to the MgO(110) substrate.

All heterostructure samples were characterized by x-ray reflectivity (XRR) to determine the layer thicknesses and interfacial roughnesses. The XRR curves (see figure 1) were fitted using the GenX software package [16] and the resulting fitting parameters for a four-layer model are given in table 1. As expected, the roughness of the epitaxial FePt layer is low with a root mean square value (σ) of a few Å. The subsequent (bottom), as well as the final (top) NiFe layers consistently show a roughness of order 10 Å, which is also the NiFe roughness found for the Mn-free sample, except for the 5 and 10 Å-thick Mn spy layer samples. In these latter cases, the NiFe roughness doubles (∼22 Å), which goes hand-in-hand with the roughness of the Mn interlayer being on the order of the thickness of the layer itself (∼4.5 Å and ∼8 Å, respectively). The 10 Å Mn control sample on Pt shows a similarly rough Mn layer, however, the NiFe interface below appears not to be affected.

To study the heterostructure in more detail, and to gain insight into the interfaces between Mn and its adjacent layers, an additional sample with a 15 Å-thick Mn layer was studied by cross-sectional transmission electron microscopy (TEM) in a JEOL JEM-2100 microscope operated at 200 kV. The TEM samples were prepared by conventional methods that include mechanical thinning and Ar ion milling. Figure 2(a) shows a high-resolution TEM overview of the layer stack, clearly resolving the MgO(110) substrate, the FePt layer, as well as the NiFe stack with the Mn interlayer in the middle. In

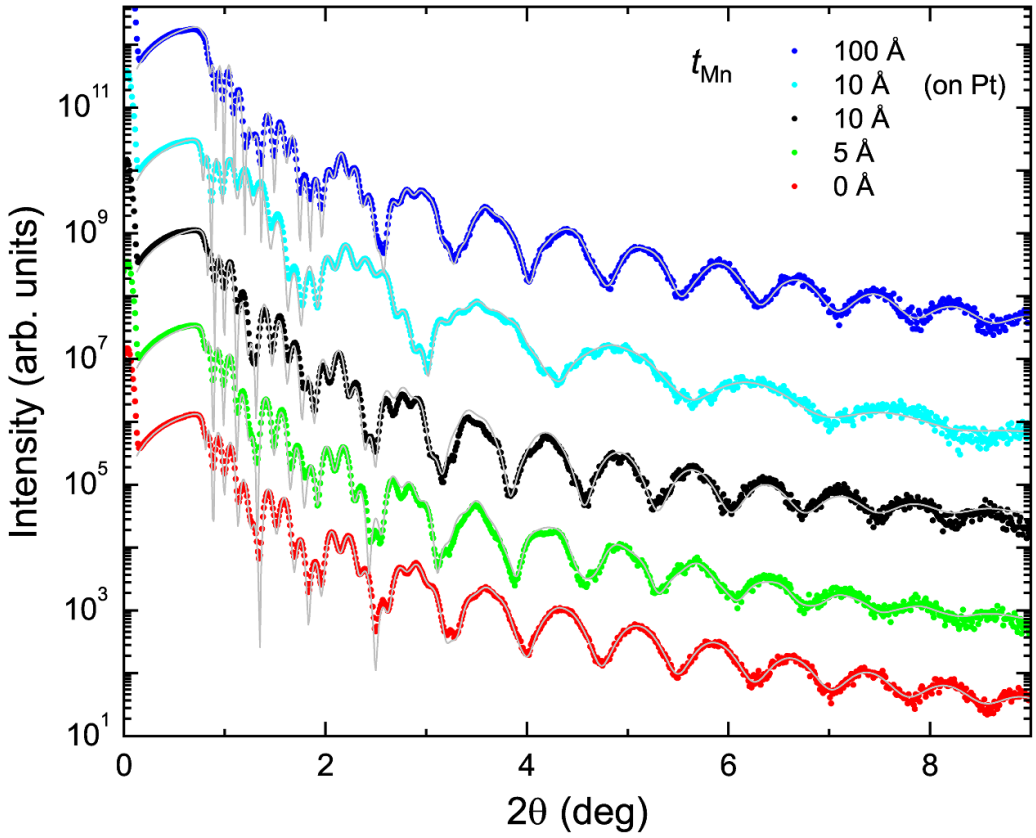

Figure 1. XRR measurements performed on the sample series. The measured data points are represented by (colored) dots and the fitted plots by gray lines. The plots have been vertically shifted for clarity. The lower three curves were obtained from the MgO(110)/FePt(100 Å)/NiFe(200 Å)/Mn(t_{Mn})/NiFe(200 Å) samples, while the upper two curves were obtained from the MgO(110)/Pt(50 Å)/NiFe(200 Å)/Mn(t_{Mn})/NiFe(200 Å) reference samples.

Table 1. Film thicknesses and roughnesses obtained from GenX fits to the XRR data shown in figure 1. The samples are categorized by their nominal Mn thickness. All film thicknesses t and roughnesses σ (root mean square roughness) are given in Å. The * symbol indicates the sample for which the FePt layer was replaced by a Pt layer.

Sample	FePt (*Pt)		NiFe		Mn		NiFe	
t_{Mn}	t	σ	t	σ	t	σ	t	σ
0	114	3.30	377	10.6				
5	118	3.84	193	23.0	5.0	4.5	188	10.4
10	119	2.47	197	22.3	8.2	8.4	196	11.3
10*	63.9	4.11	187	11.4	8.48	7.3	191	10.0
100	113	3.17	182	5.70	166	7.3	181	7.31

figures 2(b) and (c), close-ups of the upper NiFe layer and the vicinity of the Mn layer are shown, respectively. From the distance of the fringes visible in the images, atomic layer spacings of 1.8 Å for the NiFe layer and ∼2.2 Å for Mn are obtained. We note that the diffractogram does not show the (100) spot, as would be expected for $L1_0$ ordered FePt. Its absence is the result of the combined contributions of kinematic and dynamic electron diffraction effects [17]. To determine all lattice spacings and the crystallographic relationships between the layers, we analyzed the diffractogram (obtained from the large-scale overview shown in the inset to figure 2(d)). The diffractogram shows diffraction spots from MgO, FePt, and Py. They are all aligned with the MgO substrate peak (the (200) and (220) spot are labeled), i.e. all layers are epitaxial. The (200) lattice spacings are 2.1 Å (MgO), 1.9 Å (FePt), and 1.8 Å (NiFe).

To characterize the in-plane magnetic anisotropy, hysteresis loops were obtained by vibrating sample magnetometry (VSM) with the magnetic field applied at different orientations within the plane of the film. Element-specific XMCD hysteresis loops were also acquired to identify the magnetization state of the different layers in the samples. VNA-FMR measurements were performed to identify the resonant modes, while XFMR measurements were used to evaluate the magnetization dynamics of the different magnetic elements within the structure.

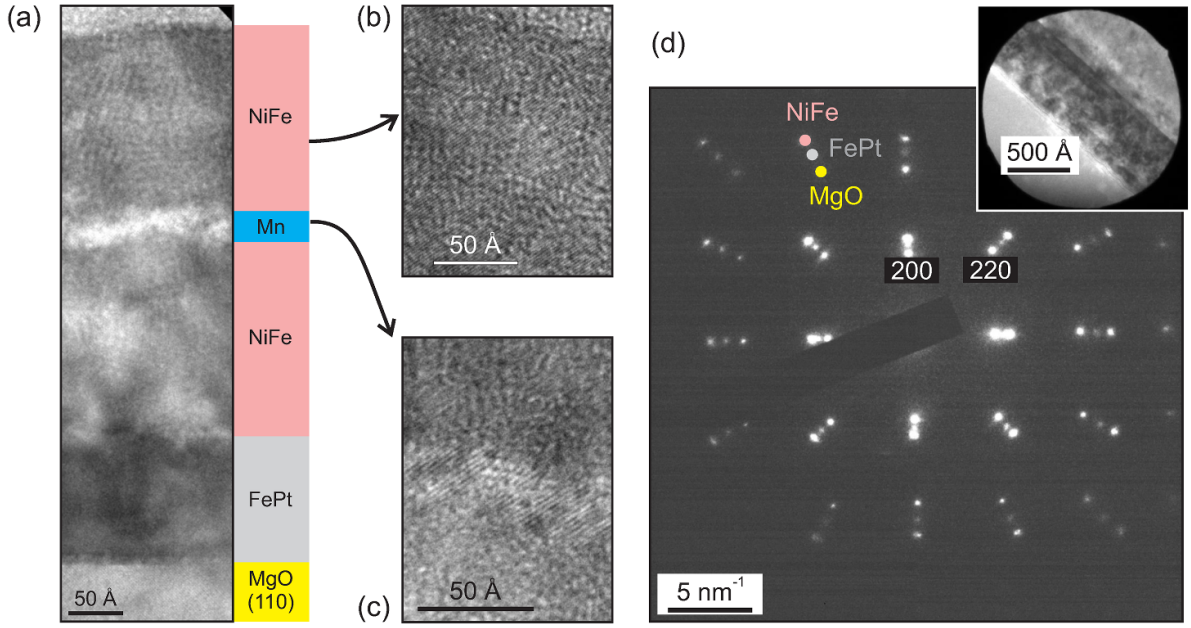

Figure 2. (a) High-resolution TEM image of the layer stack, showing the MgO(110) substrate, the FePt, lower NiFe, Mn, and upper NiFe layers. (b), (c) High-resolution TEM image of the upper NiFe layer and the NiFe/Mn/NiFe interface region, respectively. (d) Diffractogram of the overview TEM image shown as an inset. The NiFe and FePt layers are highly epitaxial, following the orientation of the MgO substrate.

XMCD and XFMR measurements were conducted in the portable octupole magnet system (POMS) end station on the I10 beamline at the Diamond Light Source (UK). X-ray absorption measurements were made using circularly polarized x-rays at the Fe, Ni, and Mn $L_{2,3}$ absorption edges in transmission geometry in luminescence yield mode, i.e. the x-ray excited optical luminescence from the MgO substrate is detected by a photodiode mounted behind the sample. The XMCD gives a measure of the element-specific magnetic moment along the direction of the x-ray beam, which was along the applied field [18]. For the XFMR measurements, circularly polarized x-rays were used to probe the magnetization while precession was induced by a radio frequency (rf) magnetic field, which was perpendicular to the applied bias field [19]. The rf frequency was synchronized to a harmonic of the synchrotron master oscillator clock (~500 MHz) for stroboscopic measurements. Changing the delay between the rf field and the x-ray pulses (delay scan) allows the amplitude and phase of the signal to be extracted by fitting to a sinusoidal function. Moreover, field scans, where the bias field is scanned for a fixed time delay, were then combined with the delay scans to fully characterize the dynamics for a given rf frequency (6 and 8 GHz in the present case) [20–24].

3. Results and discussion

3.1. Static measurements

VSM hysteresis loops (figure 3) were acquired with an in-plane (IP) applied magnetic field at different angles θ_H relative to the [001]-axis of the substrate. The FePt/NiFe bilayer without a Mn spy layer behaves as a single rigid magnet due to the interlayer exchange coupling between the FePt and NiFe. The coercivity at $\theta_H = 0°$ is 4 mT. For $\theta_H = 90°$, the saturation field of 80 mT is the result of the significant IP uniaxial anisotropy of the FePt layer, although values of up to an order of magnitude larger have been previously reported for similar FePt/NiFe structures [14]. Adding the NiFe layer decreases the hard axis saturation field of a single FePt layer (deposited in the same way; not shown) from 400 mT to 80 mT. The relatively modest uniaxial anisotropy of the FePt may be the reason why loop shapes characteristic of ES formation [20, 25] are not observed for the $\theta_H = 0°$ easy axis case, where the magnetization prefers to switch as a 'single unit'. However when the field is applied in-plane and perpendicular to the easy axis of the FePt layer, a twisted magentization state is set up. Here, the FePt magnetization remains aligned close to its easy axis, while the soft NiFe layer becomes twisted. The calculated magnetization curve for this twisted magnetization state is shown by the red line in figure 3(b), and is in good agreement with the experimental data. The parameters used for this calculation were derived from the 'fits' to the VNA-FMR data presented below (section 3.2).

For $t_{Mn} = 5$ Å, the loops show a single switching event for $\theta_H = 0°$, indicating that the entire sample remains ferromagnetically coupled. With increasing θ_H, at least two switching events become apparent which may be attributed to the Mn layer decoupling the NiFe layers above and below it. This suggests that $t_{Mn} = 5$ Å is beyond the limit for which the static magnetization of the FePt/NiFe host is unaffected by the presence of the Mn spy layer. The hysteresis loops rule out the possibility of noncollinear Mn moments [26] since the extended higher field hysteresis loops saturate at low fields and show no additional switching at higher fields.

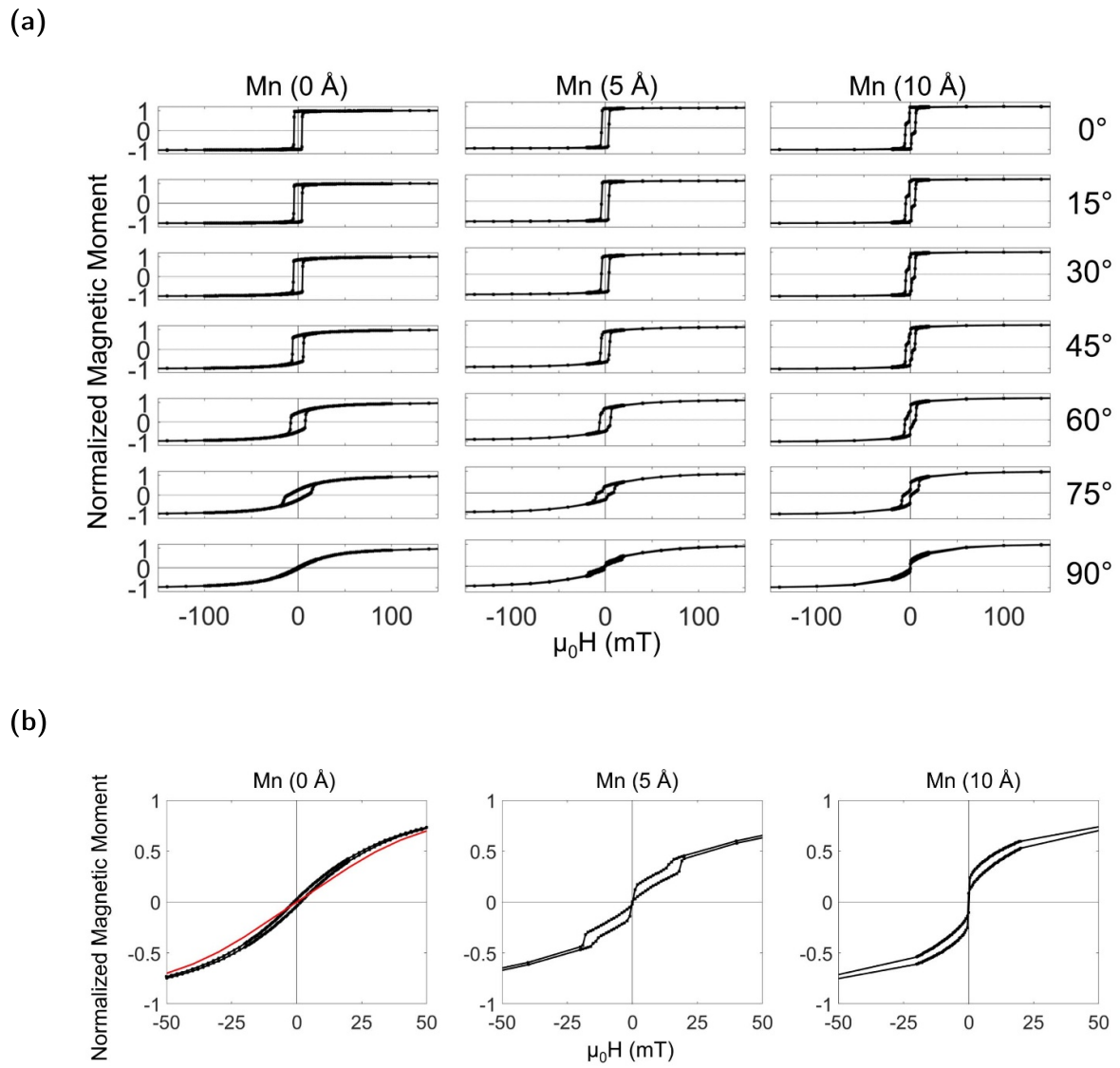

Figure 3. (a) Vibrating sample magnetometer hysteresis loops obtained for samples with $t_{Mn} = 0$, 5, and 10 Å. The angle describing the orientation of the applied magnetic field within the (110) plane is measured relative to the [001] direction, and reaches a value of 90° when the field is parallel to the [$\bar{1}$10] direction. (b) An enlarged view of the hard axis (90°) VSM loops from (a). The calculated curve for the $t_{Mn} = 0$ Å case assumes a twisted magnetization state and is shown by the red line.

The XMCD loops for Ni, Fe, and Mn for $\theta_H = 0°$ (figure 4) show distinct behaviors depending on the Mn thickness. For $t_{Mn} = 5$ Å, the Ni and Fe loops retain the square shape observed for the $t_{Mn} = 0$ Å sample. The switching of all three atomic species occurs at the same field value, showing that the NiFe and FePt magnetizations are parallel for all field values, further suggesting that ferromagnetic coupling occurs through the Mn layer.

For $t_{Mn} = 10$ Å, the Ni and Fe XMCD loops display two separate switching events, suggesting that the Mn here decouples the NiFe layer in which it is embedded, into a lower layer ($NiFe_L$) which is adjacent to the FePt layer, and an upper NiFe layer ($NiFe_U$). The Ni XMCD signal is very similar for the two plateau regions, in which the $NiFe_U$ and $NiFe_L$ moments are antiparallel, as the applied field is swept up and down, as expected since the $NiFe_U$ and $NiFe_L$ layers contain similar amounts of Ni. The offset of the plateaus in the Fe XMCD signal indicates that the $NiFe_U$ switches before the $FePt/NiFe_L$, which contains the larger amount of Fe, as the field is reduced from saturation. The loop for the Mn layer has an unexpected shape with the signal magnitude being largest between the switching fields seen in the Ni and Fe loops.

Theoretical studies predict that when Mn is deposited on metallic substrates, different couplings to adjacent layers may occur at the upper interface compared to deeper lying Mn layers [27]. An asymmetric roughness profile [28] was observed in NiFe/FeMn/NiFe trilayers and attributed to greater interdiffusion at the upper FeMn/NiFe interface.

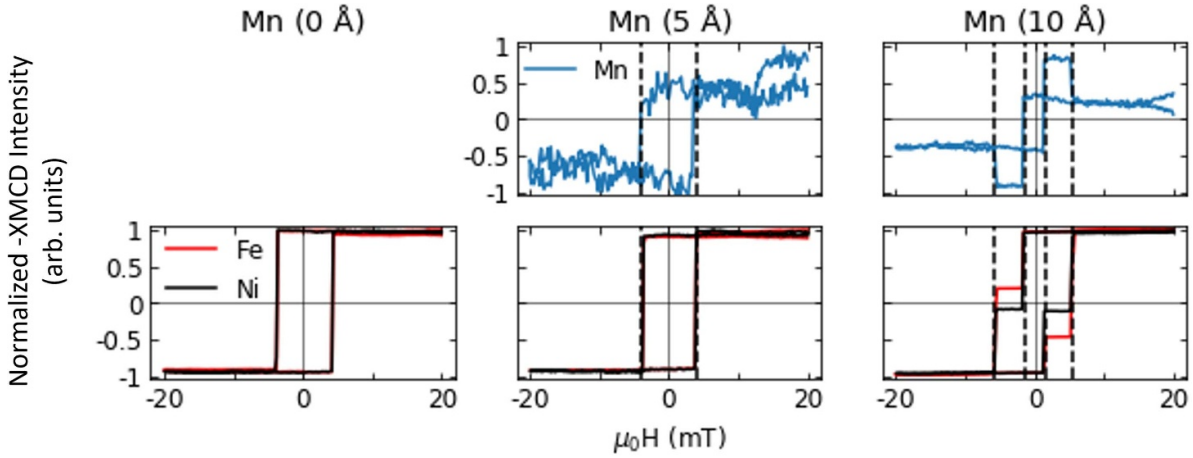

Figure 4. Normalized element-specific -XMCD hysteresis loops for the $t_{Mn} = 0$, 5, and 10 Å samples (from left to right) with the field applied along the in-plane easy axis $\theta_H = 0°$. The Ni (black) and Fe (red) data are shown in the bottom panels and the Mn hysteresis (blue) in the top panels.

Parallel, antiparallel or no magnetic coupling between Mn and Fe moments are all possible [29], resulting from different growth conditions such as sputtering pressure [30], as well as oxygen contamination [31]. This sensitivity could lead to different Mn interlayer exchange coupling mechanisms at the different Mn/NiFe interfaces. In the present growth series, for thin Mn layers the interface with the lower NiFe layer was observed to be heavily distorted. The Mn layers of nominally 5 and 10 Å thickness had a roughnesses of the same order. For the heterostructure involving FePt, the roughness of the lower NiFe layer almost doubled, whereas this increase is less for the Pt-based heterostructure. A likely scenario is that Pt acts as a diffusion barrier for Mn, whereas FePt does not, which means that Mn diffuses all the way through the lower NiFe layer.

An explanation of the observed Mn XMCD loop shape is illustrated in figure 5. The measured Mn magnetic moment is assumed to be the sum of moments associated with sublayers at the top and bottom of the deposited Mn layer. Three regimes are identified as the field is swept from negative to positive saturation. In regime (1), all moments are aligned parallel to the external field except for that of the lower Mn sublayer which lies antiparallel to the applied field. The moment of this sublayer is antiferromagnetically coupled to the FePt/NiFe below and the (upper) Mn/NiFe above. Application of a small reverse field switches the moment of the upper Mn/NiFe layer while the lower Mn layer remains pinned by the FePt/NiFe layer. In this field regime (2), the moment of the lower Mn layer is subject to competing couplings to the layers above and below, with the coupling to the FePt/NiFe below being dominant. As the applied field is swept further, regime (3) is reached when the FePt/NiFe and the lower Mn moment both switch and the system enters the positive high field state where all moments are reversed relative to those in field regime (1).

The origin of the two Mn rich regions with distinct moments was explored through scanning transmission electron microscopy (STEM) measurements performed on an additional sample containing the same FePt and NiFe layers but with $t_{Mn} = 15$ Å. The larger Mn thickness was chosen

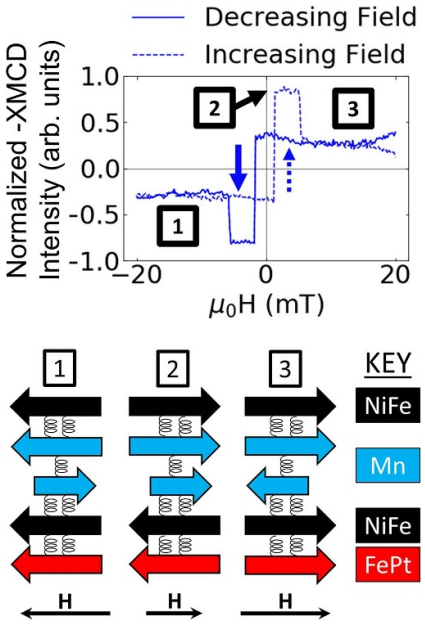

Figure 5. Model of the magnetization reversal for the $t_{Mn} = 10$ Å sample. The XMCD hysteresis loop for the easy axis ($\mathbf{H} \parallel$ MgO[001]). Different regimes within the field sweep from negative saturation to positive saturation are identified and labeled. The orientations of the different moments for each field regime are presented below. The number of adjoining springs represent the strength of the coupling between layers.

to provide a larger signal, in recognition that this thickness is at the limit of the spatial resolution of the STEM probe used here. The results, shown in figure 6, indicate that Mn remains as a single layer, eliminating the possibility of significant Mn diffusion to the top of the upper NiFe layer [32, 33] for this sample thickness. As we have shown above, for thinner Mn layers, strong interdiffusion is a likely scenario. Interdiffusion of Mn and an increased interfacial roughness at the NiFe/Mn and Mn/NiFe interfaces has been observed in similar NiFe/FeMn/NiFe [28] and Fe/Mn/Fe [34] structures,

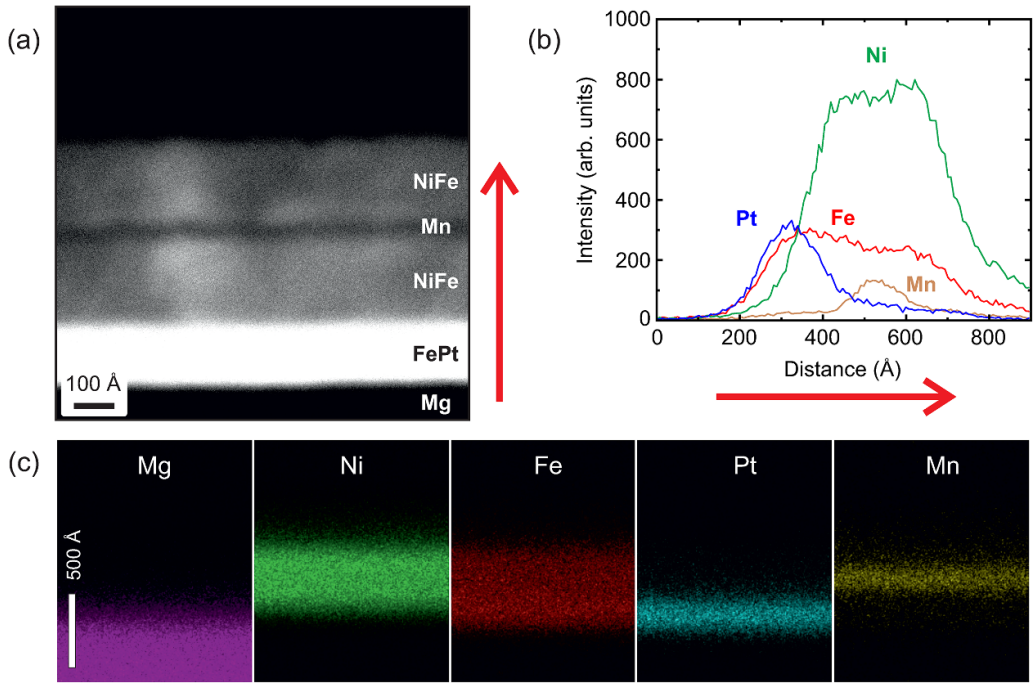

Figure 6. (a) Annular dark-field scanning transmission electron microscopy (STEM) image showing the different layers of the $t_{Mn} = 15$ Å sample. The red arrow denotes the direction of increasing distance from the interface with the MgO substrate in (b). (b) Elemental depth distribution from energy dispersive x-ray spectroscopy (EDS). The total nominal thickness of the stack is 515 Å. (c) Element distribution maps for Mg, Ni, Fe, Pt, and Mn.

suggesting two other likely scenarios. First, there is the possible formation of an interfacial NiFeMn alloy [35]. In the suggested reversal model, the moment of the upper Mn layer is ferromagnetically coupled to the upper NiFe layer, suggesting that coupling within a NiFeMn alloy is ferromagnetic. The lower Mn layer is then antiferromagnetically coupled at both its interfaces. Second, structural defects within the Mn layer [36] could lead to grains hosting different magnetic phases, giving rise to distinct Mn moments. Based on the frequent observation of NiFeMn alloy formation [32, 35, 37] and the asymmetry of the Mn line profile in figure 6(b), we believe that formation of an interfacial NiFeMn alloy at the upper Mn/NiFe interface is the more likely scenario for the thicker Mn spy layers. We would like to acknowledge that the sensitivity of the Mn state to growth conditions, particularly temperature and oxidation [26, 29], has been established in previous experiments and invites further study to identify the universality of the asymmetric NiFeMn formation and subsequent effects for other sample conditions.

3.2. *Dynamic measurements*

To investigate the influence of the Mn spy layer on the magnetization dynamics of the FePt/NiFe bilayer, VNA-FMR measurements were first performed with the static magnetic field applied along the hard [$1\bar{1}0$] and easy [001] axis directions, respectively. XFMR measurements were then performed with the static field parallel to the hard [$1\bar{1}0$] axis to explore the dynamical response of the different elemental species.

The magnitude of the S_{21} scattering matrix component extracted from VNA-FMR measurements is shown in figure 7. A single resonance is observed for any given field value. With the static field applied parallel to the easy axis in figure 7, the frequency increases monotonically with increasing field for all three samples. With the field applied parallel to the hard axis in figure 7, for $t_{Mn} = 0$ Å, a transition is observed between two modes at an induction field of ∼150 mT that corresponds to the saturation value of the corresponding hysteresis loop in figure 3. For $t_{Mn} = 5$ and 10 Å, a continuous 'W' shaped variation of the resonance frequency is instead observed. The frequency minima occur at induction field values of ∼100 and 60 mT for $t_{Mn} = 5$ and 10 Å, respectively, that are in rough agreement with the saturation fields observed in the hysteresis loops.

The element-resolved dynamics detected by XFMR are presented in figure 8. The field values at which resonance peaks are observed are in good agreement with the values at which resonance occurs in figure 7, as highlighted by the horizontal blue lines that correspond to the frequencies at which XFMR measurements were made. Furthermore, the same resonances are observed for Ni, Fe, and Mn, with a similar phase of precession for each element.

An initial understanding of the VNA-FMR data of figure 7 can be obtained by thinking of the sample as a single homogeneous NiFe slab with uniaxial magnetic anisotropy and effective magnetic parameters [39]. With the static field applied parallel to the in-plane easy axis, in figure 7, the zero-field resonance frequency varies noticeably between the three samples.

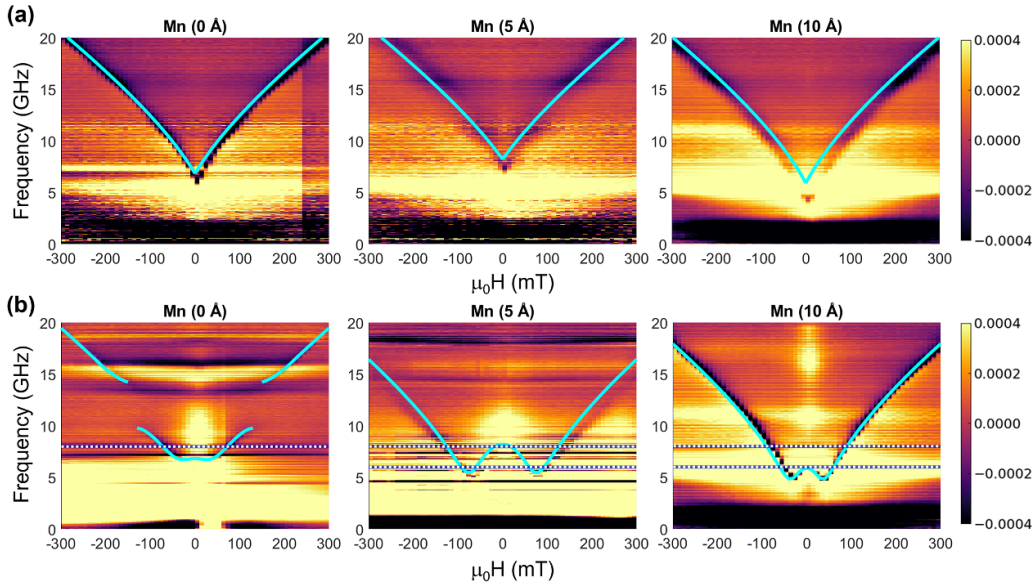

Figure 7. Magnitude of the S_{21} scattering matrix component from VNA-FMR measurements with the static field applied parallel to (a) the [001] easy and (b) [1$\bar{1}$0] hard axis, sweeping from positive to negative field. The left, middle, and right columns correspond to the 0, 5 and 10 Å Mn samples, respectively. The horizontal white dashed lines in (b) indicate the frequencies used in XFMR measurements. Fits to a multilayer model [38] are shown as light blue lines and are discussed in the main text.

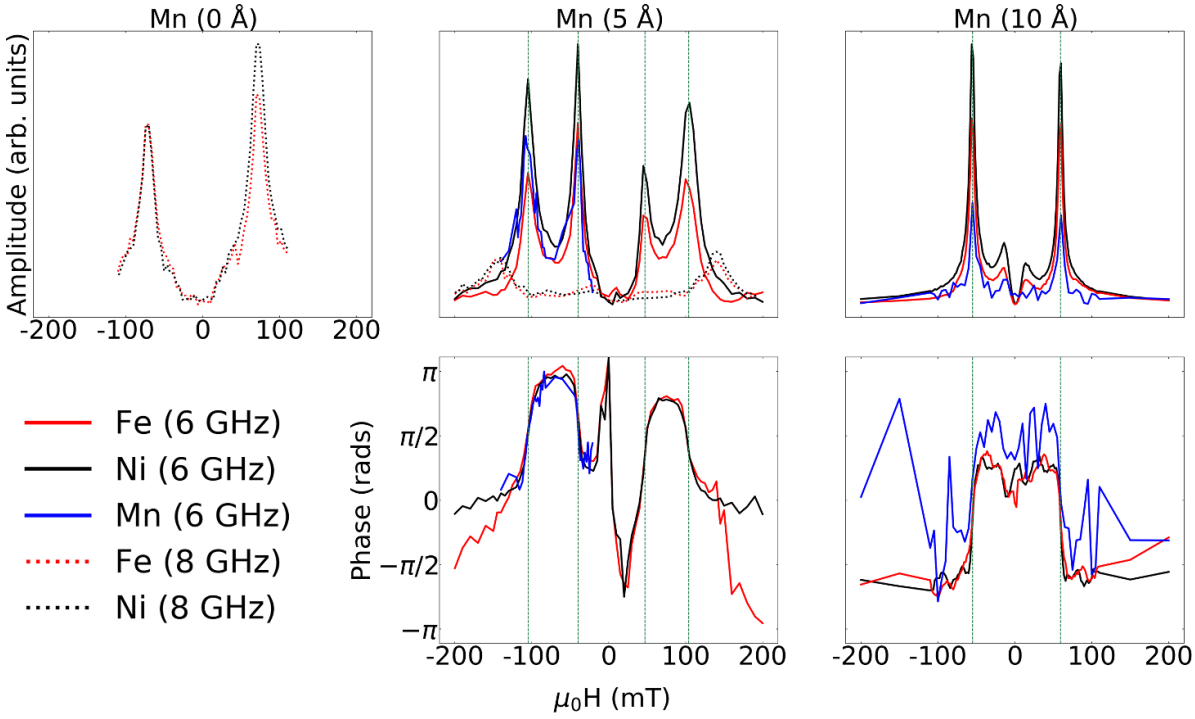

Figure 8. Amplitude and phase of XFMR field scans measured at the frequencies indicated in the legend. Amplitudes for Ni (black), Fe (red), and Mn (blue) have been scaled for ease of comparison, with solid (6 GHz) and dashed (8 GHz) lines representing the two different frequencies used. In the lower panels, the phase of the XFMR signal measured at 6 GHz for the $t_{\mathrm{Mn}} = 5$ and 10 Å samples is shown. The vertical lines indicate the resonance fields.

The different values can be interpreted as being due to differences in the size of the effective uniaxial anisotropy imprinted by the FePt pinning layer. Although the FePt layer is nominally identical in each case, variations in uniaxial anisotropy may result from small variations in the substrate and growth conditions.

With the static field applied parallel to the in-plane hard axis, in figure 7, the samples with 5 and 10 Å thick Mn lay-

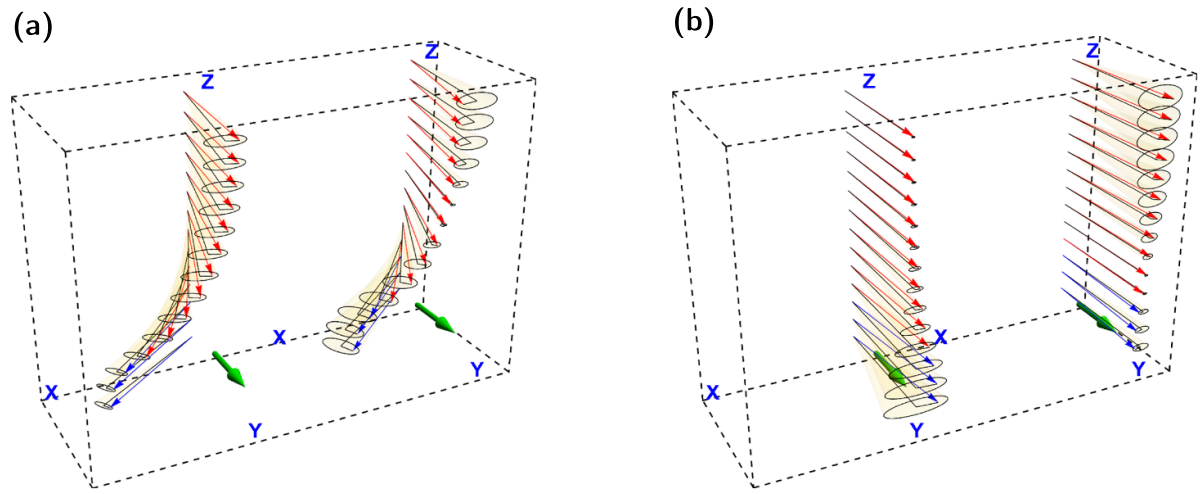

Figure 9. Schematic diagram on the left (right), of the uniform (first exchange) mode of a FePt/NiFe bilayer (as for $t_{Mn} = 0$ Å) with static magnetic field (green arrow) applied parallel to the hard axis. The assumed field strength is (a) 100 mT (below the anti-crossing at ∼150 mT) and (b) 300 mT (above the anti-crossing at ∼150 mT). The simulation parameters are as stated in the main text. Magnetization vectors are shown for every 14th discretization layer with FePt and NiFe vectors shown in blue and red respectively. Diagrams for further field values are included as an animation within a supplementary file.

ers exhibit a frequency minimum at the saturation field, as might be expected for a homogeneous layer. As the field strength is decreased from high values, the resonance frequency decreases, but then increases again as the magnetization cants away from the hard axis as the field strength is decreased below the saturation value. However, for the sample without a Mn layer, a qualitatively different behavior is observed. Instead, an anti-crossing between two different modes occurs at the saturation field.

An improved understanding can be obtained from a 1D multilayer model that yields both the uniform mode and higher order (exchange modes) of a FePt/NiFe bilayer. The model of Dąbrowski *et al* [38] has been generalized to include exchange parameters λ_{NiFe} and λ_{FePt}, and anisotropy parameters K_{NiFe} and K_{FePt} for the NiFe and FePt layers, respectively, and an exchange parameter λ_{Inter} to describe their interfacial coupling. Within this model, the magnetization vectors are left free to vary. The NiFe exchange parameter was fixed at $\lambda_{NiFe} =$ 214 K [38]. To reduce the number of free parameters in the model, the exchange constants for NiFe and FePt were set to the same value. In fact, the model is not particularly sensitive to the precise value of λ_{FePt} because, in this layer, the spins are essentially ferromagnetically aligned. The NiFe and FePt slabs were discretized into $N_{NiFe} = 150$ and $N_{FePt} = 38$ layers, respectively, and used to calculate the light blue curves in figure 7.

The samples with 5 and 10 Å thick Mn layers, which showed hard axis behavior reminiscent of a single homogeneous layer, are considered first. For the 5 Å-Mn sample, the simulations assume $\lambda_{NiFe} = \lambda_{FePt} = 214$ K, $\lambda_{Inter} =$ 1.0 K, $K_{NiFe} = -0.022$ K, $K_{FePt} = -0.2$ K,$\mu_0 M_{FePt} = 1.00$ T, and $\mu_0 M_{NiFe} = 1.00$ T, with all energies specified in degrees Kelvin. For the 10 Å-Mn sample, parameters $\lambda_{NiFe} = \lambda_{FePt}$ = 214 K, $\lambda_{Inter} = 1.0$ K, $K_{NiFe} = -0.01$ K, $K_{FePt} = -0.2$ K, $\mu_0 M_{FePt} = 1.00$ T, and $\mu_0 M_{NiFe} = 1.05$ T were used. In each case, λ_{Inter} is greatly reduced relative to λ_{NiFe} and λ_{FePt}, such that the NiFe and FePt layers are almost decoupled from each other. In fact, the minimum frequency of the W-shaped curve is strongly dependent on the value of λ_{Inter}, with the minimum frequency dropping to zero when $\lambda_{Inter} = 0$ (so-called soft-mode behavior). The minimum frequency is also sensitive to misalignment of the applied field from the hard axis direction. However, a plausible experimental error of ∼2° in the field orientation leads to change of ∼50% in the deduced value of λ_{Inter}, while still remaining two orders of magnitude smaller than the values of λ_{NiFe} and λ_{FePt}. Reduced interfacial coupling at the FePt/NiFe would lead to switching of the NiFe layers at reduced field values, as is indeed seen in the hard axis VSM hysteresis loops. Diffusion of Mn through the lower NiFe layer and into the FePt, as suggested by analysis of the XRR data, may be why the exchange coupling is quenched at the FePt/NiFe interface.

For the 0 Å-Mn sample, the simulation assumes $\lambda_{NiFe} =$ $\lambda_{FePt} = \lambda_{Inter} = 214$ K, $K_{NiFe} = -0.009$ K, $K_{FePt} = -0.12$ K, $\mu_0 M_{FePt} = 1.00$ T, and $\mu_0 M_{NiFe} = 1.05$ T. Here, there is strong exchange coupling across the FePt/NiFe interface but the anisotropy of the FePt layer is somewhat smaller. In fact, the reduced anisotropy is responsible for a soft-mode behavior in the simulations at a field value of 0.21 T as the FePt magnetization begins to cant away from the applied field. The presence of a such a soft-mode dictates that the frequency of the uniform mode, primarily associated within the NiFe layer at low field, increases initially with the applied field, but then falls to zero when the field strength reaches 0.21 T. The beginning of the downturn, at the anti-crossing field at ∼0.12 T, can be seen. Concomitant with this behavior, there is an upturn in the frequency of the first exchange mode, which is primarily associated with the FePt layer at low field, but moves into the NiFe layer above the anti-crossing. The spatial character of the uniform and first exchange modes is shown in figures 9(a)

and (b), at fields below and above the anti-crossing, respectively.

The spatial profiles presented in figure 9 explain why only one mode is observed in the experimental data of figure 7. At the lower field value of 100 mT, the spatially uniform microwave field couples to the lower frequency mode that has uniform phase through the bilayer stack, but not to the higher frequency mode where the phase changes by π radians through the thickness of the bilayer. On the other hand, at the higher field of 300 mT, the microwave field couples strongly to the higher frequency mode that is confined largely within the NiFe layer where it has uniform phase. While the microwave field can in principle also couple to the lower frequency mode, it is confined predominantly within the FePt layer where the much larger damping leads to an increased linewidth such that the mode is not resolved within the measurement.

It should also be noted that the values of the anisotropy parameters K_{NiFe} of -0.022 K for the 5 Å Mn sample, and -0.009 K for the 0 Å Mn sample, correspond to uniaxial anisotropy induction fields of about 0.024 T and 0.010 T, respectively. Both values are an order of magnitude larger than those typically observed for NiFe, and suggest that the uniaxial anisotropy may be enhanced by a combination of interfacial strain and diffusion of Mn into the NiFe layer.

Finally, we note that the suggested model for the reversal of the 10 Å-Mn sample requires two distinct Mn rich regions, yet only one resonance mode can be observed within the Mn XFMR data. Since the Mn XFMR signal is in phase with that of Fe and Ni for both $t_{\mathrm{Mn}} = 5$ and 10 Å, the XFMR signal must originate from the Mn region that has its magnetization parallel to that of Fe and Ni, i.e. the interdiffused NiFeMn layer. This is consistent with the model presented in figure 5 since the pure Mn layer is absent for $t_{\mathrm{Mn}} = 5$ Å. For $t_{\mathrm{Mn}} = 10$ Å, the Mn-rich layer with magnetization antiparallel to that of NiFe is expected to precess with reduced amplitude and so makes little contribution to the net XFMR signal.

4. Conclusions

This work has explored whether an ultrathin Mn layer can act as a 'spy layer' for static and dynamic magnetization within FePt/NiFe bilayers such that a magnetic moment is induced in the Mn without disrupting the state of the host system. For both $t_{\mathrm{Mn}} = 5$ Å and 10 Å, modified hysteresis loops and ferromagnetic resonance have been observed. For $t_{\mathrm{Mn}} = 10$ Å, a model has been presented in which the Mn layer is divided into a lower Mn-rich layer and an upper interdiffused NiFeMn layer, with magnetization parallel and antiparallel to that of the NiFe host layer, respectively. Furthermore, the exchange coupling at the FePt/NiFe interface is significantly reduced in these samples, hinting at migration of Mn to the FePt/NiFe interface. Clearly, a Mn spy layer thickness of less than 5 Å is required if modification of the static and dynamic magnetic response of the host layer is to be avoided. A spy layer that inherits the magnetization of a layer at a given depth without altering the magnetic properties of the probed layer would be able to enhance the utility of XMCD-based measurements beyond existing restrictions.

Data availability statement

All data that support the findings of this study are included within the article (and any supplementary files).

Acknowledgments

The authors acknowledge the support of the Engineering and Physical Sciences Research Council (EPSRC) through Grants EP/P02047X/1, EP/P020151/1 and EP/P021190/1. D G N acknowledges support through the EPSRC Centre for Doctoral Training in Metamaterials (Grant Number EP/L015331/1). Beamtime awarded on the I10 beamline using the portable octupole magnet system (POMS) at Diamond Light Source (MM-23338) is acknowledged. The authors also acknowledge Diamond Light Source for time on the laboratory Diffractometer in their Optics Laboratories.

ORCID iDs

David G Newman https://orcid.org/0000-0002-4076-0288
David M Burn https://orcid.org/0000-0001-7540-1616
Emily Heppell https://orcid.org/0000-0002-3977-4623
Maciej Dąbrowski https://orcid.org/0000-0002-6033-5721
Gerrit van der Laan https://orcid.org/0000-0001-6852-2495
Robert J Hicken https://orcid.org/0000-0002-4788-6211

References

[1] Kneller E F and Hawig R 1991 *IEEE Trans. Magn.* **27** 3588
[2] Bowden G J, Beaujour J M L, Gordeev S, de Groot P A J, Rainford B D and Sawicki M 2000 *J. Phys.: Condens. Matter* **12** 9335
[3] Li S, Livshitz B, Bertram H N, Fullerton E E and Lomakin V 2009 *J. Appl. Phys.* **105** 07B909
[4] Seki T, Utsumiya K, Nozaki Y, Imamura H and Takanashi K 2013 *Nat. Commun.* **4** 1726
[5] Seki T, Zhou W and Takanashi K 2016 *J. Phys. D: Appl. Phys.* **49** 075002
[6] Dąbrowski M *et al* 2020 *ACS Appl. Mater. Interfaces* **12** 52116
[7] Burn D M, Zhang S L, Yu G Q, Guang Y, Chen H J, Qiu X P, van der Laan G and Hesjedal T 2020 *Phys. Rev. Lett.* **125** 137201
[8] Demangeat C and Parlebas J C 2002 *Rep. Prog. Phys.* **65** 1679
[9] Schneider A, Fu C-C and Barreteau C 2018 *Phys. Rev.* B **98** 094426
[10] Tulchinsky D, Unguris J and Celotta R 2000 *J. Magn. Magn. Mater.* **212** 91
[11] Frisk A, Achinuq B, Newman D G, Heppell E, Dąbrowski M, Hicken R J, van der Laan G and Hesjedal T 2023 *Phys. Status Solidi* a **220** 2300010
[12] Frisk A, Achinuq B, Newman D G, Dąbrowski M, Hicken R J, van der Laan G and Hesjedal T 2023 *Phys. Rev. Appl.* **20** 044027
[13] Laughlin D E, Srinivasan K, Tanase M and Wang L 2005 *Scr. Mater.* **53** 383

[14] Utsumiya K, Seki T and Takanashi K 2011 *J. Appl. Phys.* **110** 103911
[15] Ohtake M, Itabashi A, Kirino F and Futamoto M 2013 *IEEE Trans. Magn.* **49** 3295
[16] Björck M and Andersson G 2007 *J. Appl. Crystallogr.* **40** 1174
[17] Kohn A, Lazarov V K, Singh L J, Barber Z H and Petford-Long A K 2007 *J. Appl. Phys.* **101** 023915
[18] van der Laan G and Figueroa A I 2014 *Coord. Chem. Rev.* **277–278** 95
[19] Arena D A, Vescovo E, Kao C-C, Guan Y and Bailey W E 2006 *Phys. Rev.* B **74** 064409
[20] Stenning G B G *et al* 2015 *New J. Phys.* **17** 013019
[21] van der Laan G 2016 *J. Electron Spectrosc. Relat. Phenom.* **220** 137–46
[22] Marcham M K *et al* 2013 *Phys. Rev.* B **87** 180403
[23] Li J *et al* 2016 *Phys. Rev. Lett.* **117** 076602
[24] van der Laan G and Hesjedal T 2023 *Nucl. Instrum. Methods Phys. Res.* B **540** 85
[25] Shelford L R, Liu Y, Al-Jarah U, de Groot P A J, Bowden G J, Ward R C C and Hicken R J 2014 *Phys. Rev. Lett.* **113** 067601
[26] Zelený M, Sob M and Hafner J 2009 *Phys. Rev.* B **80** 144414
[27] Hafner J and Spišák D 2005 *Phys. Rev.* B **72** 144420
[28] Nascimento V, Passamani E, Alvarenga A, Biondo A, Pelegrini F and Saitovitch E B 2008 *Appl. Surf. Sci.* **254** 2114
[29] Rader O, Pampuch C, Gudat W, Carbone A D C and Eberhardt W 1999 *Europhys. Lett.* **46** 231
[30] Spenato D, Youssef J B, Le Gall H and Ostoréro J 2001 *J. Appl. Phys.* **89** 6898
[31] Andrieu S, Foy E, Fischer H, Alnot M, Chevrier F, Krill G and Piecuch M 1998 *Phys. Rev.* B **58** 8210
[32] Youssef J B, Spenato D, Gall H L and Ostoréro J 2002 *J. Appl. Phys.* **91** 7239
[33] Kim S W, Kim J K, Kim J H, Kim B K, Lee J Y, Lee S S, Hwang D G and Rhee J R 2003 *J. Appl. Phys.* **93** 6602
[34] Passamani E C, Croonenborghs B, Degroote B and Vantomme A 2003 *Phys. Rev.* B **67** 174424
[35] Blinov I V, Krinitsyna T P, Korolev A V, Matveev S A, Arkhipova N K, Milyaev M A, Popov V V and Ustinov V V 2014 *Phys. Met. Metallogr.* **115** 335
[36] Migliorini A *et al* 2018 *Nat. Mater.* **17** 28
[37] Wu C-H, Zheng C, Chiu C-C, Manna P K, van Lierop J, Lin K-W and Pong P W T 2017 *Jpn. J. Appl. Phys.* **57** 01AC04
[38] Dąbrowski M, Hicken R J, Frisk A, Newman D G, Klewe C, N'Diaye A T, Shafer P, van der Laan G, Hesjedal T and Bowden G J 2021 *New J. Phys.* **23** 023017
[39] Kittel C 2004 *Introduction to Solid State Physics* (Wiley)